Influence of Phase Transformations on the Mechanical Properties of High-Strength Austenitic Fe-Mn-Cr Steel

LIEVEN BRACKE, GEERT MERTENS, JAN PENNING, BRUNO C. DE COOMAN, MARTIN LIEBEHERR, and NURI AKDUT

The influence of Cr and N additions on the mechanical properties of a Fe-Mn-C steel was investigated. The chemical composition was found to have a pronounced effect on the strain-hardening behavior, due to the strain-induced sequence of the $\gamma \rightarrow \varepsilon \rightarrow \alpha'$ martensitic transformations. It was found that Cr and N suppress this transformation sequence. At Cr levels higher than 7.5 mass pct, no α' martensite was formed, which led to a pronounced improvement of the ductility. The differences in transformation behavior can be attributed to the change in the intrinsic stacking-fault energy (ISFE): in the compositional range studied, Cr and N additions cause an increase of the ISFE.

I. INTRODUCTION

COMPARED to ferritic steels, austenitic steel grades have much better strength-ductility properties. Tensile strengths of over 800 MPa, combined with elongations of over 50 pct, are readily achieved. The low intrinsic stacking-fault energy (ISFE) of austenitic steels inhibits easy cross slip, thereby increasing the strain-hardening rate. Moreover, some austenitic ferrous alloys can transform into martensite, which further leads to enhanced strain hardening. These effects delay necking and are very effective in increasing both the strength and ductility of the material.

For specific applications, *e.g.*, automotive structural parts that must absorb the impact energy during a crash event, a combination of high strength and ductility is desirable. The most important indicators for the way a structural member can absorb energy are the yield strength and the strain-hardening coefficient of the material it is made of. It is favorable to have a sustained degree of strain hardening during the deformation. There are several options available to achieve this type of behavior. A first possibility is standard transformation-induced plasticity (TRIP), where austenite transforms to α' martensite during deformation, thus, locally hardening the material and preventing further deformation and necking in the deformed region. This type of behavior is observed, *e.g.*, in the meta-stable stainless austenitic-grade AISI 301 or low-alloy C-Mn-Si TRIP steels. Another option to achieve a high strain-hardening rate is through mechanical twinning, *i.e.*, twinning-induced plasticity. In this case, austenite forms very thin mechanical twins, which results in smaller-sized grains by grain segmentation. The present study makes it possible to compare differences in transformation and twinning behavior during deformation and relate these differences to the mechanical properties of the alloys studied.

Most austenitic steels are stainless (Cr $>$ 12 pct) and use Ni as the main austenite-stabilizing element. The Cr content can be lowered for the intended application, because the forming properties of the steel are more important than its corrosion resistance. Alternatives for the Ni additions include Mn, C, and N. In this work, the properties of five different Fe-18Mn-0.25C alloys with varying amounts of Cr and N were studied. In binary Fe-Mn austenitic steels containing less than 30 mass pct of Mn, the microstructure contains both austenite and martensite. The martensite is mainly α' martensite (bcc/bct) at low Mn contents and ε martensite (hcp) at higher Mn contents. Schumann[1] studied the martensite-start temperatures in the binary Fe-Mn system and found that austenite and α' martensite are the phases present at room temperature for alloys with up to 15 pct Mn. Between 15 and 27 pct Mn, the microstructure consists of ε martensite and austenite, while alloys with over 27 pct Mn are fully austenitic. Both α' martensite and ε martensite can be thermally induced, stress induced, or strain induced.

The formation of strain-induced ε martensite is usually explained using the model illustrated in the schematic representation shown in Figure 1. In fcc metals and alloys with a low ISFE, an intrinsic stacking fault originates from the dissociation of a perfect dislocation into two Shockley partials. An example of a possible dislocation reaction is given in Formula [1].

$$\frac{a}{2}\left[\bar{1}10\right] \rightarrow \frac{a}{6}\left[\bar{1}2\bar{1}\right] + \frac{a}{6}\left[\bar{2}11\right] \qquad [1]$$

When the first Shockley partial moves through the material, the stacking sequence of the close-packed planes in the fcc structure changes. This can be presented as follows. Consider the ABCABCABC stacking of close-packed planes in fcc metals and the ABABAB stacking in hcp metals. When a Shockley partial dislocation passes through a B plane and a C plane in the material, the slipped material is shifted in such a way that a C plane comes into the original A position, an A plane comes into the original B position, and a B plane comes into the original C position. This means that a small area with hcp stacking is formed within the fcc material, which is an intrinsic stacking fault. By a suitable pole mechanism, identical partial dislocations on every second {111} lattice plane, with respect to its neighbors, can move through the fcc mother phase and generate a thin ε-martensite plate.

Putaux and Chevalier[2] have shown that thermally induced ε martensite always grows in three different variants, each

LIEVEN BRACKE and GEERT MERTENS, Graduate Students, JAN PENNING and BRUNO C. DE COOMAN, Full Professors, are with the Department of Metallurgy and Materials Science, Ghent University, Ghent, Belgium. Contact e-mail: Lieven.Bracke@Ugent.be MARTIN LIEBEHERR, Senior Research Engineer, and NURI AKDUT, Manager Stainless Steel Research, are with the Arcelor Industry Research Laboratory, Zelzate, Belgium.

Manuscript submitted January 24, 2005.

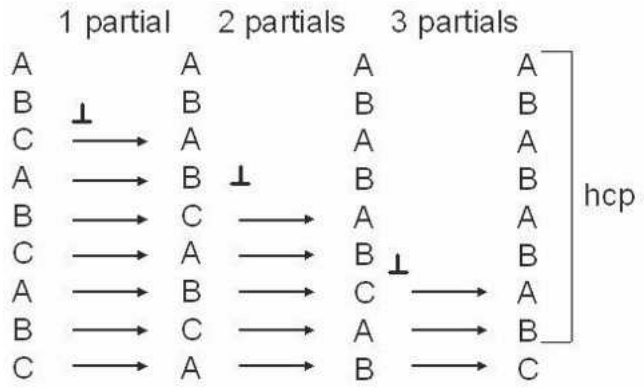

Fig. 1—Schematic representation of the stacking fault–based model for the ε-martensite nucleation.

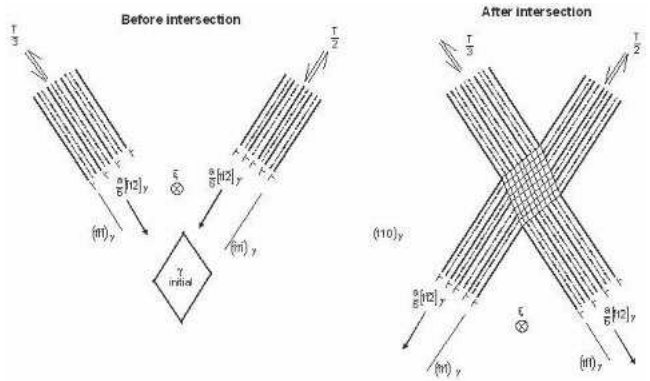

Fig. 2—Schematic illustration of the nucleation of α′ martensite at the intersection of deformation bands in austenite.[4]

related to another set of Shockley partials on the same close-packed plane, in order to minimize the transformation strains in the austenite. Strain-induced ε martensite grows by the multiplication of only one type of Shockley partial on the close-packed plane, namely, the one which is oriented preferentially with respect to the applied deformation.

An intrinsic stacking fault can be considered to be a thin, four-lattice-plane thick, ε-martensite crystal. If slip on every second close-packed plane is considered, a sequence of intrinsic stacking faults forms a large hcp region forming the ε-martensite plates. It is clear that the ISFE of the material, which is proportional to the chemical driving force ($\Delta G^{\gamma-\varepsilon}$) for the ($\gamma-\varepsilon$) transformation,[3] will be an important parameter in the probability to form ε martensite. A low ISFE implies that stacking faults can readily be formed in the austenite, so it can be expected that a low ISFE promotes the presence of ε martensite. As mentioned before, both thermally and strain-induced α′ martensite can also be formed in Fe-Mn–based alloys. Strain-induced α′ martensite can nucleate at the intersection of deformation bands in austenite. Olson and Cohen described the principle of α′-martensite nucleation at intersections of slip bands in austenite,[4] based on the model for the transition of an fcc lattice into a bcc lattice, originally proposed by Bogers and Burgers.[5] The mechanism is illustrated in Figure 2. According to the Bogers–Burgers model, the shear needed to transform an fcc lattice into a bcc lattice can be divided into two invariant-plane strains, which can take place successively or simultaneously. The first component corresponds to one-third of the twinning shear in an fcc lattice with a displacement of $a_{fcc}/18 <112>$. This is denoted as T/3 in Figure 2. This T/3 shear can be achieved by an array of $a_{fcc}/6 <112>$ Shockley partial dislocations, averaging one over every third $\{111\}_{fcc}$ glide plane. The second shear component corresponds to one-half of the twinning shear in an fcc lattice, denoted as T/2 in Figure 2. The displacement, in this case, can be described by $a_{fcc}/12 <112>$ when referring to the fcc lattice and $a_{bcc}/8 <110>$ when referring to the bcc lattice. Similar to the T/3 shear, the T/2 shear can be accomplished by an array of $a_{fcc}/6 <112>$ Shockley partial dislocations, averaging one over every second {111} plane in this case. It is clear from the model for ε-martensite formation that this T/2 shear is an alternative way to describe the formation of an hcp structure. It should be noted, however, that the exact T/2 shear is valid for a hard-spheres model. This implies that a shuffle of the atoms over $a_{fcc}/12 [1\bar{1}\bar{2}]$ on every second basal plane of the ε martensite is needed to form the exact T/2 structure. It can be shown that this shuffle transforms the $(10\bar{1}1)_{hcp}$ plane, on which the dislocations are most likely to glide in ε martensite, into a uniformly distorted $(1\bar{1}\bar{1})_{fcc}$ plane. If the T/3 partial dislocations piled up at the interface of the ε-martensite lath pass on these uniformly distorted planes, the result will be a perfect bcc structure. A commonly observed form of α′-martensite nucleation at intersections is the case with two intersecting ε-martensite laths.[4] As argued before, this is easy to fit into the model for the T/2 shear, since only a small shuffle of atoms is needed to form a perfect T/2 sheared region from ε martensite. This is not so evident for the T/3-shear case. Olson and Cohen present two possibilities to solve this problem. The first option is that it can be assumed that the strain-induced ε martensite is heavily faulted, so that there exist regions where the local average shear matches the shear of a T/3 partial dislocation array. The second option is for the case of relatively perfect ε-martensite laths. In such a case, the T/3 shear can be achieved when one-third of the dislocations trying to pass into the T/2 sheared region stay behind at the interface. This mechanism would then provide a semicoherent interface. The T/3-T/2 shear intersection can also be applied for other intersections of sheared regions in fcc metals, *e.g.*, the intersection of an ε-martensite lath intersecting an fcc twin boundary. As the α′ martensite has a larger volume per atom than austenite, the model implies considerable coherence strains in the austenite. It can be expected that these coherency strains will be relaxed through plastic deformation and possibly a rigid-body rotation. This may influence the orientation relationship between the different phases.

An important parameter influencing the amount of α′ martensite and ε martensite is the ISFE. It has been reported that ε martensite can be formed when the ISFE is lower than 15 to 20 mJm^{-2}.[4,5] Allain *et al.*[8] have found that the strain-induced $\gamma-\varepsilon$ transformation can occur for ISFE values lower than $18 mJm^{-2}$ and that mechanical twinning can occur for ISFE values between 12 and 35 mJm^{-2}. The influence of alloying elements on the ISFE is not unambiguous. It depends on the type and concentration of other alloying elements.

In the binary Fe-Mn system, Mn has been reported to lower the ISFE at low concentrations. For higher concentrations, Mn results in an increase of the ISFE, as is shown in Figure 3.

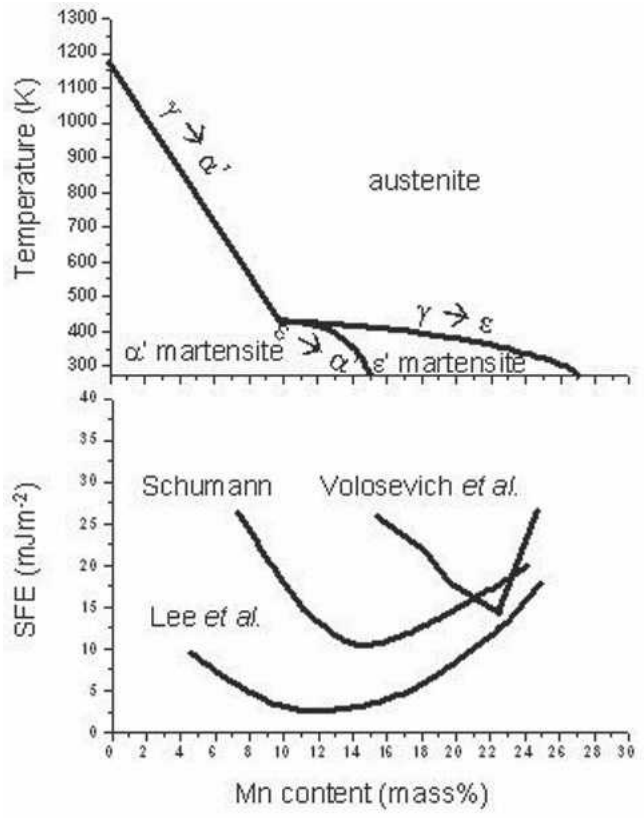

Fig. 3—Evolution of stacking-fault energy at room temperature according to Schumann,[6] Lee *et al*.,[9] and Volosevich *et al*.[10] The phase composition in the binary Fe-Mn system as proposed by Schumann[1] is also shown.

Schumann found a minimum value of 12 mJm^{-2} for a Mn content of 14 pct,[6] while Lee *et al*. found a value of 3 mJm^{-2} for a Mn content of 13 pct.[9] Volosevich *et al*. found a minimum value of 15 mJm^{-2} at 22 pct Mn.[10] Lee *et al*. have questioned the validity of the data reported by Volosevich.[9]

The influence of Cr on the ISFE of austenitic ferrous alloys is mainly known from studies carried out on the Fe-Cr-Ni system. Cr lowers the ISFE in this system when its content is lower than 20 pct.[9,10,11] According to Rhodes and Thompson, the following equation is applicable for the ISFE of Fe-Cr-Ni alloys with Cr levels lower than 20 pct:[13]

$$\text{ISFE}\ (mJm^{-2}) = 17.0 + 2.29Ni - 0.9Cr \qquad [2]$$

For alloys with Cr additions higher than 20 pct, the ISFE is given by[13]

$$\text{ISFE}\ (mJm^{-2}) = -26.6 + 0.73Ni + 2.26Cr \qquad [3]$$

Schramm and Reed investigated the influence of low quantities of C, N, Si, and Mn on the ISFE in the Fe-Cr-Ni system,[14] with Cr and Ni contents varying from 8.5 to 30 pct, resp. 9.43 to 24.7 pct. They report the following ISFE expressions (Eqs. [4a] through [4d]):

$$\text{ISFE}\ (mJm^{-2}) = 4 + 1.8Ni - 0.2Cr + 410C \quad \text{C: 0.012 to 0.027 pct} \qquad [4a]$$

$$\text{ISFE}\ (mJm^{-2}) = 34 + 1.4Ni - 1.1Cr - 77N \quad \text{N: 0.004 to 0.044 pct} \qquad [4b]$$

Table I. ISFE for Fe-Cr-Ni with Different Si Additions, as Presented in Reference 15

Ni (Mass Pct)	Cr (Mass Pct)	Si (Mass Pct)	ISFE (mJm^{-2})
14.1	17.8	0.01	50
14.0	17.7	0.90	32
13.55	17.4	1.86	26
13.75	17.2	2.79	22
13.70	17.1	3.66	21

$$\text{ISFE}\ (mJm^{-2}) = 34 + 2.2Ni - 1.1Cr - 13Si \quad \text{Si: 0.01 to 0.59 pct} \qquad [4c]$$

$$\text{ISFE}\ (mJm^{-2}) = 32 + 2.4Ni - 1.2Cr - 1.2Mn \quad \text{Mn: 0.001 to 1.56 pct} \qquad [4d]$$

Thomas and Henry[15] made a study on the effect of Si additions on the ISFE in the Fe-Cr-Ni system. Their results, as presented in Table I, show clearly that Si additions lower the ISFE markedly.

Adding large amounts of Mn to the Fe-Cr-Ni system changes the influence of Cr on the ISFE: instead of lowering the ISFE with increasing Cr levels, the ISFE increases. Rhodes and Thompson propose a formula for the ISFE that is applicable for Fe-18Cr-9Ni–type alloys with considerable amounts of Mn and Si:[13]

$$\text{ISFE}\ (mJm^{-2}) = 1.2 + 1.4Ni + 0.6Cr + 17.7Mn - 44.7Si \qquad [5]$$

In the case of Fe-Ni-Cr alloys with large contents of Mn and Mo, the ISFE is given by[16]

$$\text{ISFE}\ (mJm^{-2}) = -53 + 6.2Ni + 0.7Cr + 3.2Mn + 9.3Mo \qquad [6]$$

The element N is also known to have a pronounced influence on the ISFE. Additions of N higher than ~0.2 pct are expected to lower the ISFE, according to References 11, 19, and 20. The ISFE decreases from 53 to 33 mJm^{-2} when the N content increases from 0.21 to 0.24 pct in Cr21Ni6Mn9 alloys. Further increasing the N content does not significantly influence the ISFE. The ISFE was also reported to increase for N additions up to 0.4 pct and to decrease for higher levels.[17] Some authors find an increase in ISFE with N additions, depending on the N content and on the presence of other alloying elements, like Cr, Ni, Mn, Si, and C. An example is given by Petrov,[21] who reported that increasing the N content from 0.05 to 0.23 pct in an austenitic Cr13Mn19 steel led to an increase of the ISFE from 320 to 400 mJm^{-2}. Gavriljuk *et al*. have given an excellent review of the available data.[12]

Jiang *et al*. added 5.3 pct Cr and 0.05 pct N to an Fe-30Mn-6Si shape-memory alloy,[16] both resulting in an increased ISFE.

II. EXPERIMENTAL PROCEDURE

The chemical compositions of the five FeMnCr alloys used for the present work are given in Table II. The main interest lies in determining the influence of the chemical

Table II. Chemical Composition (Mass Pct) of the Studied Alloys

Alloy	Mn	Cr	C	N	Si
No-Cr	17.7	—	0.25	0.084	0.29
Low-Cr	16.2	5.6	0.25	0.114	0.14
Medium-Cr	19.0	7.7	0.24	0.157	0.23
Medium-Cr + Si	19.5	7.4	0.24	0.152	1.73
High-Cr	19.0	9.7	0.24	0.196	0.24

composition on the mechanical properties of these alloys. Cr and N were added to increase the ISFE. The Si additions were expected to reduce it.

The Cr-free alloy was cast as a 1-ton slab in a laboratory continuous caster. The other alloys were prepared in a laboratory induction furnace and cast into ingots of 30 kg. After rough rolling to 25 mm, the materials were reheated to 1523 K and hot rolled on a laboratory strip mill. The hot rolling was done in five passes to a final thickness of 3 mm. The finishing temperature was kept higher than 1223 K in all cases. The hot-rolled strip was cooled from 923 K to room temperature in 12 hours and annealed at 1323 K for 15 minutes. After the annealing treatment, the recrystallized material was water quenched.

Tensile tests were carried out at room temperature on test gage bars with a width of 12.5 mm and a length of 50 mm. The strain rate applied was $16.7 \times 10^{-3}\ s^{-1}$ for deformation up to 2 pct. At a strain of 2 pct, the strain rate was increased to $20 \times 10^{-2}\ s^{-1}$. The tensile machines used were an Instron 5569 apparatus for the no-Cr and low-Cr alloys and an Instron 4505 apparatus for the other alloys. All tests were performed at room temperature.

The fracture surfaces were studied in a Zeiss DSM 962 scanning electron microscope (SEM) operated at 20 kV.

The X-ray diffraction (XRD) measurements were carried out using a Siemens 5000 diffractometer, using Mo K_α radiation ($\lambda = 0.070926$ nm) at 50 kV and 50 mA. The scanning speed applied was 0.1333 deg/min, in steps of 0.02 deg. The quantitative phase determination was done using the direct comparison method.[22] The lattice parameter of austenite was determined using the Nelson–Riley method.[23]

The volume fraction of α' martensite in the different materials was determined by magnetic saturation measurements using a LakeShore 480 fluxmeter, schematically represented in Figure 4. Introduction of a sample in the measuring coil will result in magnetization of the sample (J_m) which gives rise to a tension pulse (U_{ind}). The induction is then proportional to the integral of this pulse: $J_m \propto \int U_{\text{ind}}\, dt$. The theoretical value of the induction if the whole sample were ferromagnetic (J_{th}) is given by Eq. [7]:

$$J_{th} = J_S^{Fe} - \sum_i \alpha_i A_i \qquad [7]$$

where

J_S^{Fe} = intrinsic induction of pure Fe in a saturated condition (T),
α_i = the specific coefficient for alloying the element i (T), and
A_i = the fraction of alloying element i.

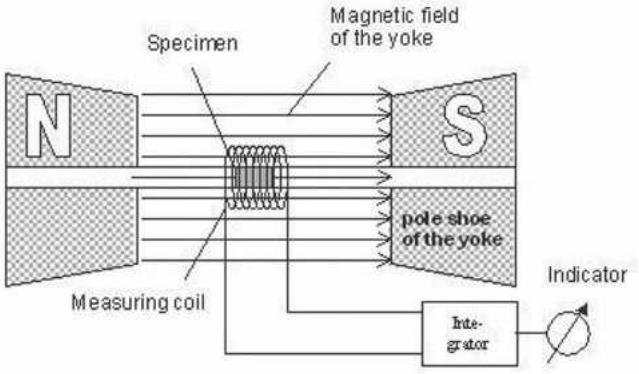

Fig. 4—Schematic representation of a magnetic saturation measurement setup.

The volume fraction of the magnetic fraction is the amount of α' martensite, since austenite is paramagnetic and ε martensite is anti-ferromagnetic at room temperature. This fraction is given by Eq. [8]:

$$f^{\alpha'} = \frac{J_m}{J_{th}} \qquad [8]$$

Thin-foil transmission electron microscopy (TEM) analysis was carried out on a PHILIPS* EM420 apparatus, operated at 120 kV. High-resolution transmission electron microscopy (HRTEM) was carried out on a JEOL** F2200 apparatus with a CEOS Cs corrector operated at 200 kV. Samples were prepared through electrolytical polishing with a solution of 95 pct CH_3COOH + 5 pct $HClO_4$ at a temperature of 12.5 °C and a voltage of 50 V.

*PHILIPS is a trademark of Philips Electronic Instruments Corp., Mahwah, NJ.

**JEOL is a trademark of Japan Electron Optics Ltd., Tokyo.

The sample preparation for the light optical metallography consisted of mechanical polishing, electrolytic polishing (solution: 90 mL distilled water, 730 mL ethanol, 100 mL butylcellosolve, and 78 mL perchloric acid), and etching (aqueous solution: 1.2 pct $K_2S_2O_5$ and 0.5 pct NH_4HF_2) to reveal the microstructural features.

The kinetics of the α'-martensite transformation was described using the model developed by Olson and Cohen,[24] which permits calculation of the fraction of strain-induced α' martensite.

$$f^{\alpha'} = 1 - \exp(-\beta(1 - \exp(-\alpha\varepsilon))^n) \qquad [9]$$

where

$f^{\alpha'}$ = the fraction of α' martensite,
α = a strain-independent constant representing the rate of shear-band formation,
β = a coefficient proportional to the probability that an intersection of shear bands will generate a nucleus,
n = an exponent accounting for the nonlinear relationship between the amount of shear bands formed and the number of intersections (n accounts for the autocatalytic effect),
ε = the Von Mises equivalent plastic strain, and

$1 - \exp(-\alpha\varepsilon)$ = the strain-dependent volume fraction of shear bands in the austenite. [10]

The Olson and Cohen model can also be used in the special case of ε martensite, since this type of martensite can be seen as a specific type of shear band, as is clear from the model for α'-martensite nucleation presented earlier.

Hecker *et al*. pointed out that the Von Mises equivalent strain has to be used in the model to obtain the most reliable result.[25] The Von Mises equivalent strain for uniaxial deformation is given by the following expression:

$$\bar{\varepsilon}_{VM} = \sqrt{\frac{2}{3}((\varepsilon_{11})^2 + (v_{22}\varepsilon_{11})^2 + (v_{33}\varepsilon_{11})^2)} \qquad [11]$$

where

ε_{VM} = the Von Mises equivalent strain,
ε_{11} = the strain in the tensile direction,
v_{22} = the Poisson coefficient in the transverse direction, and
v_{33} = the Poisson coefficient in the normal direction.

III. RESULTS

A. *Microstructural Analysis*

1. *As-produced conditions*

Figure 5 shows the microstructures of the five alloys after hot rolling and annealing. Except for the no-Cr alloy, all micrographs show a fully recrystallized austenitic microstructure. In the no-Cr alloy, ε martensite can be seen as straight black lines running across the entire austenite grain. The presence of ε martensite in this alloy was confirmed by XRD measurements, as shown in Figure 6. These diffractograms show austenite peaks for all materials, with a small ε-martensite peak for the no-Cr alloy only.

2. *Strain-induced martensitic transformation*

During tensile deformation, the alloys partially transformed from austenite to ε martensite and to α' martensite. The lattice parameters of the austenite in the as-produced condition and the ones of the ε martensite after tensile testing are presented in Table III. From these data, it is also clear that a contraction along the *c*-axis takes place, since the interplanar distance (d_{0001}) between the close-packed planes in the ε martensite is smaller than the interpanar distance (d_{111}) for the close-packed planes in the austenite. Figure 7 shows a HRTEM image of ε martensite and twinned austenite in the low-Cr alloy after 5 pct tensile deformation. This image illustrates that the ε martensite grows coherently on the close-packed {111} planes of austenite, which is in agreement with the earlier-described orientation relationships. An example of α' martensite in the no-Cr alloy is shown in Figure 8. The α' martensite has nucleated at the intersection of two ε-martensite laths and has not grown outside of the area restricted by the ε-martensite laths. The observed orientation relationship obeys both the expected Bogers–Burgers relationship between α' martensite

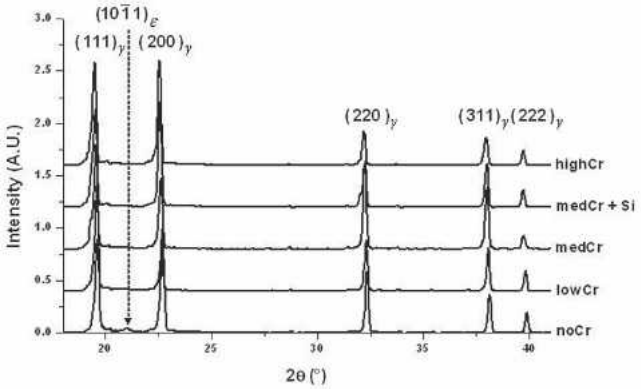

Fig. 6—XRD diffractograms in the hot-rolled and annealed condition.

Table III. Lattice Parameters for Austenite (As-Produced Condition) and ε-Martensite (after Tensile Testing)

Alloy	a_γ (nm)	d_{111} (nm)	a_ε (nm)	c_ε (nm)	d_{0001} (nm)	$c_\varepsilon/a_\varepsilon$
No-Cr	0.3599	0.2078	0.2578	0.4141	0.2070	1.6062
Low-Cr	0.3606	0.2082	0.2544	0.4118	0.2059	1.6182
Medium-Cr	0.3607	0.2083	0.2544	0.4136	0.2068	1.6252
Medium-Cr + Si	0.3609	0.2084	0.2553	0.4152	0.2076	1.6264
High-Cr	0.3607	0.2083	—	—	—	—

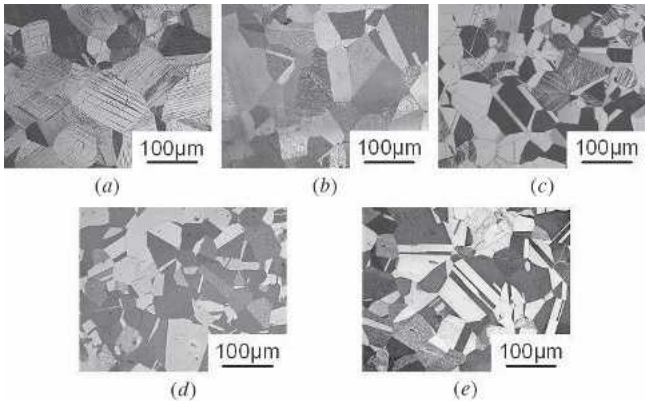

Fig. 5—Light optical micrographs after hot rolling and annealing: (*a*) the no-Cr alloy, (*b*) the low-Cr alloy, (*c*) the medium-Cr alloy, (*d*) the high-Cr alloy, and (*e*) the medium-Cr + Si alloy (etchant: aqueous solution of 1.2 pct $K_2S_2O_5$, 0.5 pct NH_4HF_2).

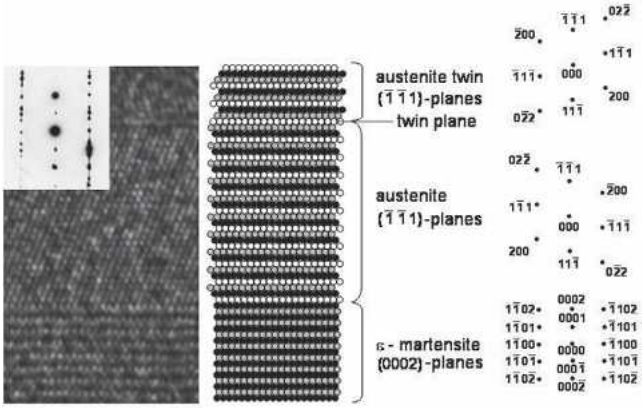

Fig. 7—HRTEM micrograph of twinned austenite and ε-martensite in the low-Cr alloy after 5 pct tensile strain. Electron beam // $[011]_\gamma$ // $[11\bar{2}0]_\varepsilon$.

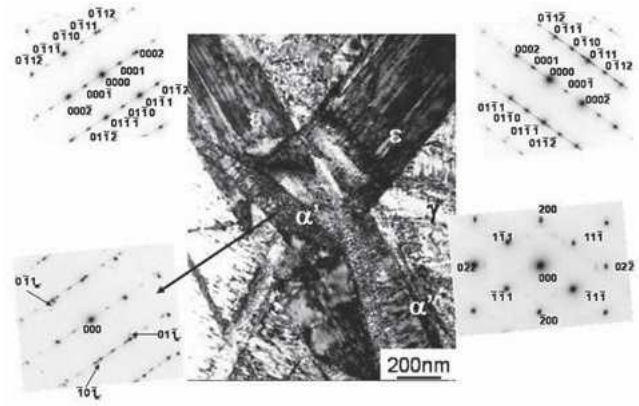

Fig. 8—TEM bright-field micrograph of the no-Cr alloy after 5 pct tensile deformation: α'-martensite on the intersection of two ε-martensite bands. Electron beam // $[011]_\gamma$ // $[2\bar{1}\bar{1}0]_\varepsilon$.

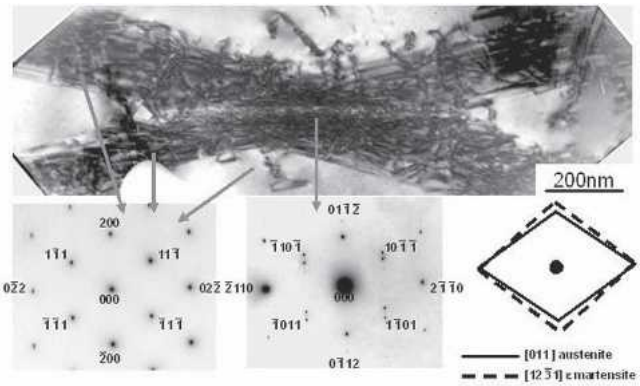

Fig. 9—TEM bright-field micrograph of the high-Cr alloy after 10 pct tensile deformation: nucleation of ε-martensite on the intersection of two deformation bands in the austenite. Electron beam // $[011]_\gamma$.

and ε martensite and the Kurdjumov–Sachs relationship between α' martensite and austenite:

$$\{111\}_\gamma // \{110\}_{\alpha'} // \{0001\}_\varepsilon$$
$$<110>_\gamma // <111>_{\alpha'} // <2\bar{1}\bar{1}0>_\varepsilon \qquad [12]$$

It is important to note that these α'-martensite islands were never observed to grow outside the area determined by the intersection region of the ε-martensite laths.

The ε martensite can be formed by the sequence of intrinsic stacking faults, as mentioned earlier, and at the intersection of two deformation bands in austenite. This is shown in Figure 9 for the high-Cr alloy after 10 pct tensile deformation. In this case, the electron beam is parallel to $[011]_\gamma$. The hcp reflections of ε martensite can be clearly observed. The ε martensite was formed on the intersection of two shear bands in the austenite, which consisted of overlapping stacking faults associated with a high density of dislocations. Although the nucleation mechanism for ε martensite is different, Relationship [12], mentioned before, again describes the orientation relationship between the two phases. In this case, however, the close packed planes that belong to the zone axis shown in the micrograph are not the planes on which the ε martensite has nucleated. A rotation of 90 deg around the $[100]_\gamma$ direction is needed to see the ε martensite edge-on.

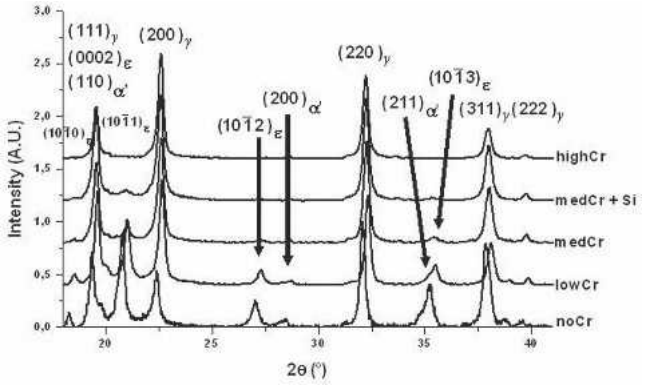

Fig. 10—XRD diffractograms after tensile testing to fracture.

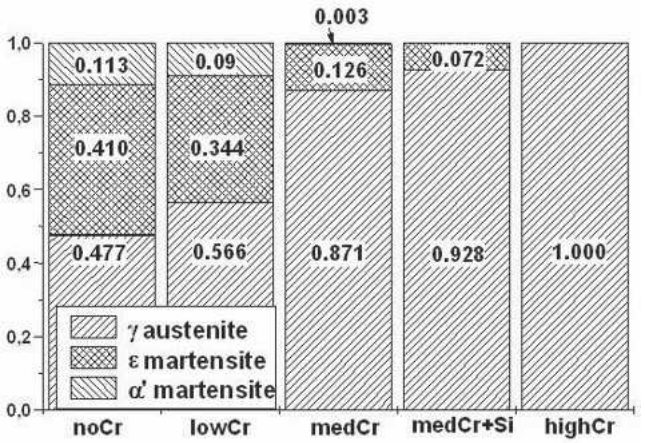

Fig. 11—Phase composition (in volume fraction) after tensile testing to fracture.

The amount of martensitic phases after tensile testing to fracture was determined by XRD (Figure 10) for the ε martensite and by magnetic saturation measurements for the α' martensite. The results are shown in Figure 11. The precise amount of ε martensite present in the material is difficult to determine exactly by means of XRD, because many diffraction peaks of austenite, α' martensite, and ε martensite overlap and must be deconvoluted. The deconvolution is made difficult due to the strong texturing resulting from the deformation. Therefore, the volume fractions of ε martensite may, therefore, not be very precise, but the tendencies certainly are, as the same peak-analysis procedure was used for all the samples. The no-Cr and low-Cr alloys show a high fraction of ε martensite and α' martensite. The medium-Cr and medium-Cr + Si alloys only exhibit ε-martensite formation. No α' martensite was observed. The TEM micrograph in Figure 12 shows the presence of microtwins in the medium-Cr alloy after tensile testing. The high-Cr alloy contains no ε martensite after fracture, but up to 10 vol pct of ε martensite was found at intermediate deformation stages. The high-Cr alloy contained microtwins after tensile testing, as is shown in Figure 13.

The evolution of the fractions of both ε martensite and α' martensite as a function of increasing strain is presented

in Figure 14 for the no-Cr and low-Cr alloys. From this graph, it is clear that increasing strain induces the formation of martensite. At low strains, the rate of ε-martensite formation is high. At higher strains, the transformation rate decreases. The decreasing rate of ε-martensite formation with strain may be caused by two phenomena. First, the amount of austenite that can transform decreases, as part of the austenite was transformed into martensite, and the remaining austenite between the martensite laths will have a smaller size. As such, the austenite is gradually stabilized against further transformation.[24,26] The second effect that reduces the rate of ε-martensite formation is the formation of α' martensite at the intersections of ε martensite.

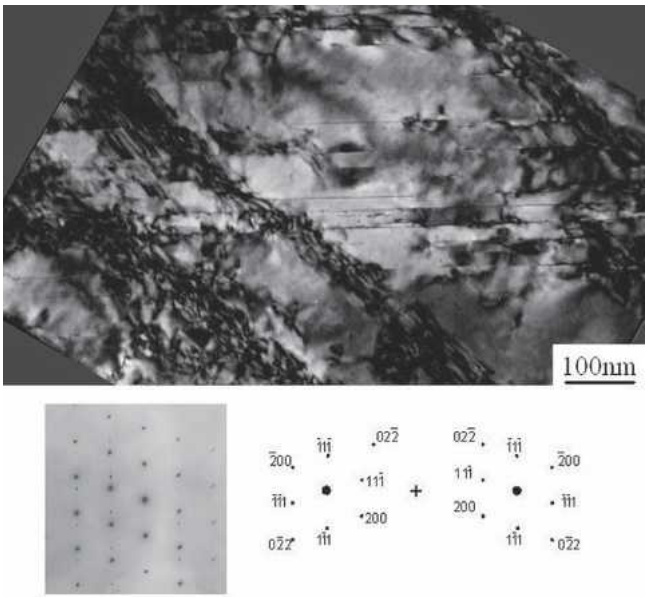

Fig. 12—TEM bright-field field micrograph of the medium-Cr alloy after tensile testing: the formation of microtwins. Electron beam // $[011]_\gamma$.

B. *Mechanical Properties*

The main mechanical properties of the alloys are summarized in Table IV. From these data, it is clear that Cr and N influence the mechanical properties of these alloys. The uniform elongation values for the no-Cr and the low-Cr alloys are equal to the total elongation, *i.e.*, there is no postuniform elongation. This is an indication of a more brittle fracture than in the case of the medium-Cr, high-Cr and medium-Cr + Si alloys. In the latter alloys, the total elongation exceeds the uniform elongation and the fracture is very ductile. This is confirmed by the study of the fracture surfaces shown in Figure 15. The medium-Cr + Si alloy clearly presents a dimpled, ductile fracture surface, whereas the no-Cr alloy presents features characteristic for a cleaved (*i.e.*, brittle) fracture surface, together with a certain amount of dimples. The low-Cr alloy is similar to the no-Cr alloy, and the medium-Cr and high-Cr alloys are similar to the medium-Cr + Si alloy.

In Figure 16, the data for the incremental strain-hardening coefficient (n_i) are presented. From these curves, it is

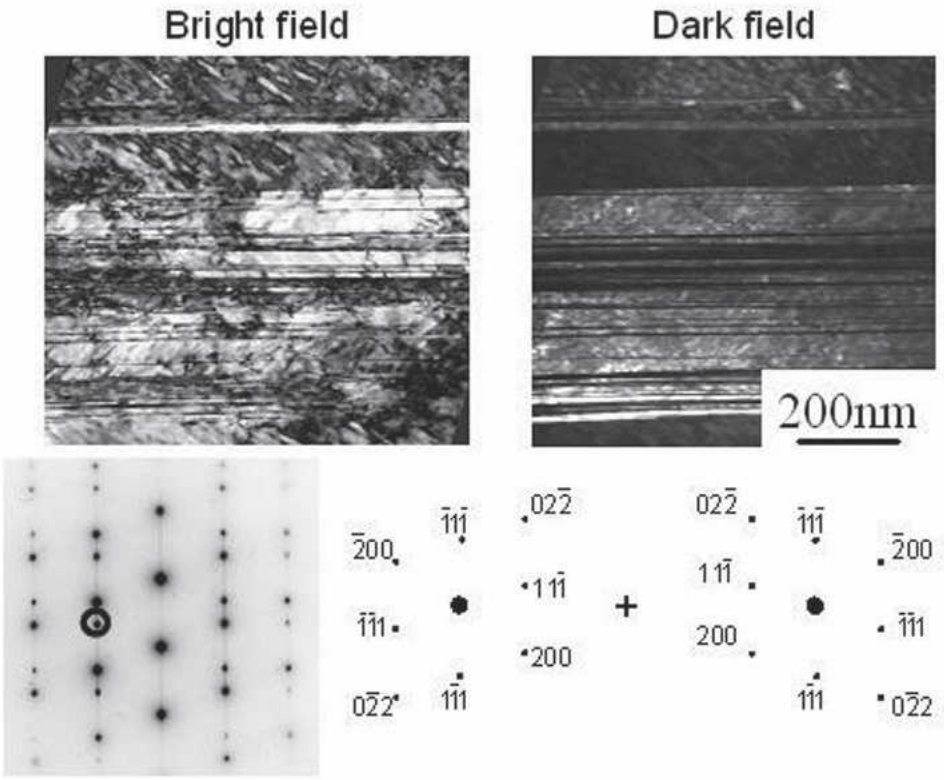

Fig. 13—TEM bright-field and dark-field micrographs of the high-Cr alloy after tensile testing: the formation of microtwins, no ε martensite observed. Electron beam // $[011]_\gamma$.

clear that the no-Cr and low-Cr alloys show a very high strain-hardening rate, while the high-Cr and medium-Cr + Si alloys have a much less pronounced strain-hardening behavior. The medium-Cr alloy has an intermediate strain-hardening value. The more gradual increase in strain hardening of the high-Cr and medium-Cr + Si alloys, in particular, should be beneficial in relation to their use as crash-resistant alloys in automotive applications. A high value of the strain-hardening coefficient can be linked to the transformation of austenite to ε martensite and/or to α' martensite. From the study of the strain-hardening curves, it is expected that the no-Cr alloy and the low-Cr alloy transform much more than the other alloys. This is confirmed by the phase analysis discussed in Section III–A–2. The high amount of martensite also reduces the ductility, as can be seen clearly in Figure 17. This behavior is very different from what is commonly observed in alloys in the meta-stable Fe-Cr-Ni system, which are characterized by a very pronounced TRIP effect. Figure 18 compares the behavior of the alloys with the commercially available AISI 301LN stainless austenitic steel grade. The no-Cr alloy shows a similar behavior to the low-Cr alloy. The medium-Cr + Si alloy shows a behavior in between that of the medium-Cr and the high-Cr alloys. The no-Cr and medium-Cr + Si alloys are not shown in Figure 18, to keep the graph clear. The AISI 301LN grade shows the well-known TRIP effect. At an engineering strain of ~0.15, the strain-induced $\gamma \rightarrow \alpha'$ transformation starts. At that point, there is a clear increase in the strength. Due to the transformation, local necking is prevented, enhancing ductility. The TRIP effect results in a high ductility, combined with a high strength. In the case of the low-Cr alloy, the transformation to ε martensite and α' martensite immediately starts and at a high rate. In this case, the strain-induced transformation apparently reduces the ductility. The high-Cr alloy does not show strain-induced transformation. Instead, deformation twinning is observed. The result is a higher ductility, but a low strength when compared to the AISI 301LN case. The medium-Cr alloy partially transforms into ε martensite during deformation. This increases the strength of the material slightly, but it also clearly reduces the elongation. From Figures 17 and 18, it is clear that the strain-induced $\gamma \rightarrow \varepsilon \rightarrow \alpha'$ transformation sequence does not result in a beneficial TRIP effect.

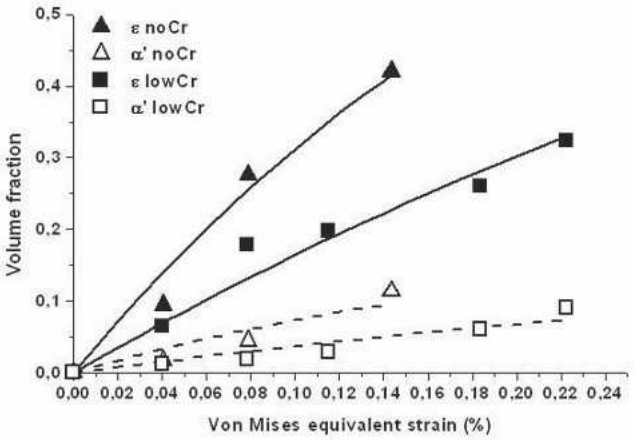

Fig. 14—Martensite volume fractions with increasing tensile strain for the no-Cr alloy and the low-Cr alloy. Data points are fitted to the Olson and Cohen equation.

Table IV. Mechanical Properties of the Alloys in the Hot-Rolled and Annealed Condition

Alloy	$R_{p0.2}$ (MPa)	R_m (MPa)	A_u (Pct)	A_{tot} (Pct)	$R_m \times A_{tot}$ (MJm^{-3})*
no-Cr	205	691	17	17	120.47
low-Cr	254	829	33	33	274.09
Medium-Cr	317	779	47	51	397.29
medium-Cr + Si	285	793	45	52	412.36
high-Cr	323	767	55	59	452.54

*In this product, A_{tot} is expressed as a fraction of the original gage length and not as a percentage.

C. *Transformation Kinetics and Modeling*

The amount of martensite as a function of strain was studied in detail for the no-Cr and low-Cr alloys. The results of

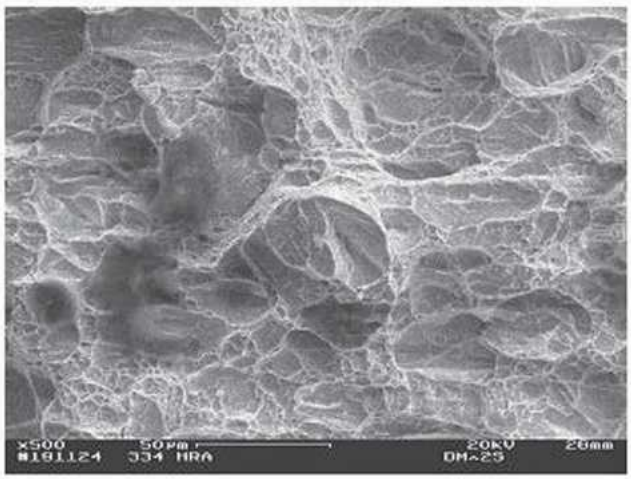

(*a*)

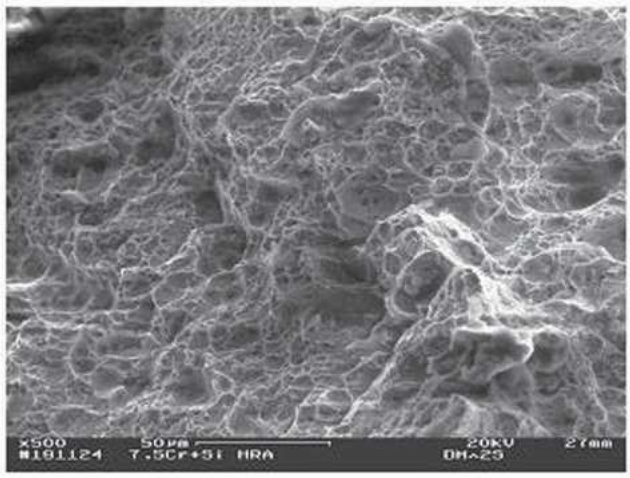

(*b*)

Fig. 15—Fracture surfaces after tensile testing: (*a*) the no-Cr alloy and (*b*) the medium-Cr + Si alloy.

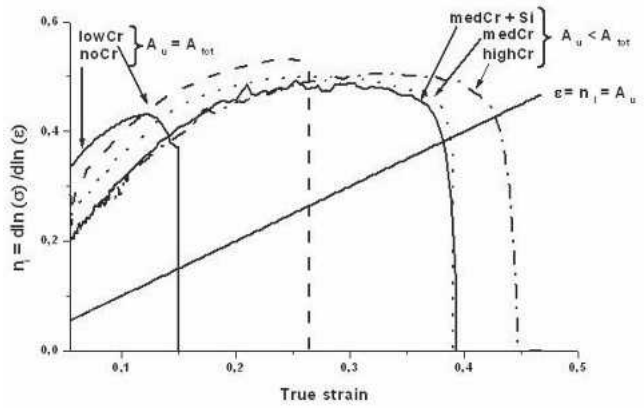

Fig. 16—Incremental strain-hardening coefficient in the hot-rolled and annealed condition.

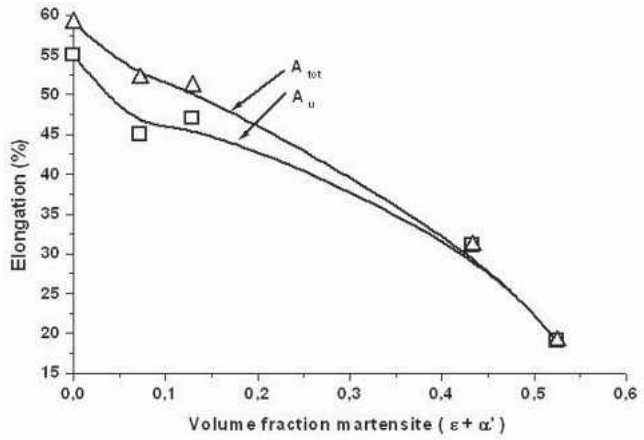

Fig. 17—Total and uniform elongation *vs* the total amount of strain-induced martensite.

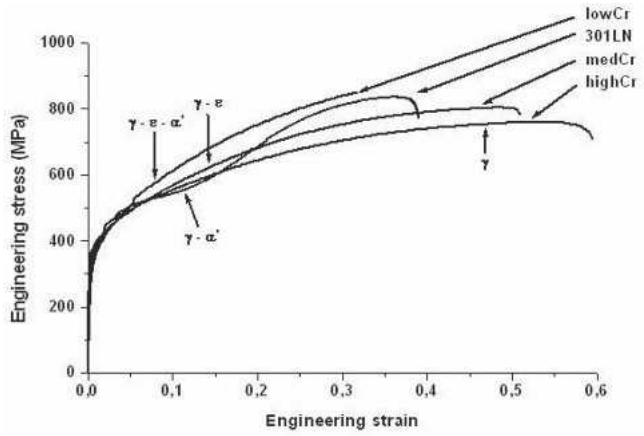

Fig. 18—Engineering stress-strain curves for the low-Cr and the high-Cr alloys not showing a TRIP effect, compared to an industrial AISI 301LN steel showing a TRIP effect.

the quantitative analysis were already presented in Figure 14. Considering that the shear bands in the Olson and Cohen model are ε-martensite laths in the case of the alloys studied, the α parameter from this model can be determined by fitting the measured amount of ε martensite to Eq. [10]. The α parameter is a measure for the rate of shear-band formation. The fitted values are $\alpha = 3.97$ for the no-Cr alloy and $\alpha = 1.76$ for the low-Cr alloy. The exponent n in Eq. [9] was set equal to 1. This exponent was introduced into the model to account for the autocatalytic effect for α'-martensite nucleation, but since it was observed that the α'-martensite islands formed did not extend beyond the ε-martensite laths, it can be expected that these α'-martensite islands will not influence the formation of new nuclei. With $n = 1$, the fitted α parameter, and the data for the volume fractions of α' martensite fitted to Eq. [9], the β value was determined. For the no-Cr alloy, $\beta = 0.24$ was found, and for the low-Cr alloy, $\beta = 0.23$. The β factor is proportional to the probability that an intersection of shear bands will generate an α'-martensite nucleus. The fact that the β factors for both alloys do not differ significantly suggests that the amount of ε martensite formed does not influence the probability that an intersection will lead to a nucleus.

IV. DISCUSSION

In the Fe-Mn-Cr-C-N alloys studied, the strain-induced transformation did not lead to an improved ductility (TRIP effect). Comparison of the transformation behavior of the present alloys with the well-documented transformation behavior of AISI 301LN may help to explain this. In the case of the no-Cr and the low-Cr alloys, the $\gamma \rightarrow \varepsilon$ transformation is initiated at low strains, as is clear from Figure 14, while at comparable strains in AISI 301LN, the flow stress remains relatively low due to the absence of transformation. The formation of ε martensite involves a smaller spacing of the close-packed planes as compared to that of the {111} planes of austenite. So, it cannot be expected that plastic instability is suppressed due to the strain-induced $\gamma \rightarrow \varepsilon$ transformation, contrary to the case of $\gamma \rightarrow \alpha'$ transformation. In the latter, the local expansion of the lattice introduces internal stresses in the austenite that operate against the applied stresses responsible for necking of the material. As such, these stresses are partially compensated at a local level, preventing the plastic instability of that area. The α' martensite is also expected to be harder than the surrounding γ phase due to the higher solid-solution hardening of C in α' martensite, as compared to in the γ *phase*. This further stabilizes the area where α' martensite is formed against deformation and necking. In the no-Cr and low-Cr alloys, α' martensite is formed as well, but in areas where these α'-martensite islands do not result in a TRIP effect, because the islands are restricted to the ε-martensite intersection where they originated. In the case of the medium-Cr and the medium-Cr + Si alloys, only the strain-induced $\gamma \rightarrow \varepsilon$ transformation takes place. Since in these cases no expansion of the lattice is present, no TRIP effect can be expected. This is confirmed by the gradual increase of the flow stress and the strain hardening, as is illustrated in the curves in Figures 16 and 18. It should be noted, however, that the strain hardening is still more pronounced than in the case of the high-Cr alloy, which does not transform. This implies that the $\gamma \rightarrow \varepsilon$ transformation contributes to the strain hardening, but not to an increase in ductility. This is likely due to the limited extent to which the hcp phase can deform (*i.e.*, a high critical resolved shear stress) and to the fact that dislocations that glide in the austenite cannot cross the

ε-martensite plates easily due to the limited availability of slip systems.

The transformation behavior of the steels studied is influenced by several parameters. The most important are the ISFE and the strength of the austenite matrix. A low ISFE implies the easy formation of intrinsic stacking faults, so the strain-induced transformation is more likely to occur, as is clear from the transformation mechanisms explained earlier. A low-strength austenite matrix implies that the strain-induced transformation will be easier, since, for the same stress level in the material, a higher strain is achieved. The grain size also plays an important role in the transformation. A smaller grain size geometrically restricts the possibilities for the transformation to occur. Since the steels studied have comparable grain sizes, there was no influence of the initial grain size on the results.

The no-Cr and the low-Cr alloys clearly have a lower yield strength than the other alloys. As the ε and α' martensites are strain-induced, the yield strength can be considered a measure for the strength of the γ matrix. Taking into account this and the fact that a lower strength of the γ matrix results in easier strain-induced transformation, it is expected that the alloys with a low yield strength will transform more readily. This is confirmed by the results for the no-Cr and the low-Cr alloys. Note that the medium-Cr + Si alloy has a lower yield strength than the medium-Cr alloy, although the medium-Cr + Si alloy transforms less. The differences in yield strength alone cannot, therefore, explain the different transformation behaviors, and other factors, *e.g.*, the ISFE, will have an important influence.

The influence of Cr and N on the ISFE can be evaluated best by comparing the medium-Cr and the high-Cr alloys. According to Allain *et al.*,[8] increasing the ISFE leads to a transition from ε-martensite formation to microtwinning during deformation. Their results indicate that strain-induced ε martensite can be formed when the ISFE is lower than 18 mJm^{-2}, while twinning can occur for ISFE values between 12 and 35 mJm^{-2}, which confirms earlier results by Schumann.[27] In the medium-Cr alloy, a considerable fraction of ε martensite was observed in combination with microtwins, while in the high-Cr alloy, microtwinning was observed without the presence of ε martensite. This indicates that the ISFE of the medium-Cr alloy can be estimated to lay between 12 and 18mJm^{-2}, while the ISFE for the high-Cr alloy has to be between 18 and 35mJm^{-2}. Since the only differences between the medium-Cr and the high-Cr alloys are the Cr and N content, it can be concluded that the combination of both elements increases the ISFE in this composition range.

Fitting the transformation kinetics to the Olson and Cohen model leads to a significantly different α parameter in the case of the no-Cr and low-Cr alloys: the no-Cr alloy has a much higher value than the low-Cr alloy. This indicates an easier formation of shear bands, considered to be laths of ε martensite in these alloys. Taking into account that α is inversely proportional to the ISFE,[24,28] it can be concluded that the no-Cr alloy has a lower ISFE than the low-Cr alloy. These two alloys differ from each other in Mn, Cr, and N content. The low-Cr alloy has 1.5 pct less Mn, 5.6 pct more Cr, and 0.03 pct more N. Mn is expected to lower rather than increase the ISFE, as is clear from Eqs. [5] and [6] and Figure 3, so the higher Cr and N levels have increased the ISFE.

The element Si is expected to significantly lower the ISFE in Fe-Mn–based alloys. So, more strain-induced ε martensite would be expected, *e.g.*, Reference 29. That is not in agreement with the results in the present work, since the medium-Cr + Si alloy transforms to a lower degree than the medium-Cr alloy. The lower amount of ε martensite after fracture in tensile testing in the medium-Cr + Si alloy is confirmed by the lower strain hardening during the deformation, as can be seen in Figure 16. Further investigation including measurement of the ISFE will be needed to explain this unexpected phenomenon.

V. CONCLUSIONS

The main conclusions of the present contribution are as follows.

1. Additions of Cr and N to an Fe-18Mn-0.25C austenitic steel result in a higher ductility and a more gradual strain-hardening behavior, which is beneficial for the deformation and gives an indication of the potential of the crash behavior of this type of steel.
2. The difference in strain-hardening behavior is due to the amount of strain-induced $\gamma \rightarrow \varepsilon$ ($\rightarrow \alpha'$) martensitic transformation. The larger the amount of transformed austenite, the more strain hardening is observed. The no-Cr and low-Cr alloys show a very pronounced strain hardening due to the $\gamma \rightarrow \varepsilon \rightarrow \alpha'$ transformation sequence. These steels show a relatively low ductility. In the high-Cr alloy, slip of dislocations is not hindered by the presence of ε martensite or α' martensite, so less strengthening and increased formability is observed. In contrast to the beneficial effect of transformation, *e.g.*, in the AISI 301LN, the alloys of the present study did not present beneficial TRIP behavior. This is due to the fact that the α'-martensite nuclei do not grow beyond the intersection of the ε-martensite laths where they are formed.
3. The main reason for the different transformation behavior is the influence of Cr and N on the stacking-fault energy: Cr and N additions result in an increase in stacking-fault energy. An increase in the stacking-fault energy limits the possibilities for intrinsic stacking faults to form, so ε- and α'-martensite formation is limited.
4. The addition of Si resulted in lower amounts of strain-induced ε martensite.

ACKNOWLEDGMENTS

The authors thank Dr. C.J.D. Hetherington, Department of Materials, Oxford University (Oxford, United Kingdom) for his efforts on the high-resolution transmission electron microscope work. The authors also acknowledge Ir. G. Lannoo at the CRM (Ghent, Belgium), for providing the no-Cr alloy and for performing the hot rolling of all the steels.

REFERENCES

1. H. Schumann: *Arch. Eisenhüttenwes.*, 1967, vol. 38 (8), pp. 647-56.
2. J.-L. Putaux and J.-P. Chevalier: *Acta Mater.*, 1996, vol. 44 (4), pp. 1701-16.

3. J.P. Hirth: *Metal. Trans. A*, 1970, vol. 1A, pp. 2367-74.
4. G.B. Olson and M. Cohen: *J. Less-Common Met*., 1972, vol. 28, pp. 107-18.
5. A.J. Bogers and W.G. Burgers: *Acta Metall*., 1964, vol. 12, pp. 255-61.
6. H. Schumann: *J. Krist. Techn*., 1974, vol. 10, pp. 1141-50.
7. B.W. Oh, S.J. Cho, Y.G. Kim, Y.B. Kim, W.S. Kim, and S.H. Hong: *Mater. Sci. Eng. A*, 1995, vol. 197, pp. 147-56.
8. S. Allain, J.-P. Chateau, O. Bouaziz, S. Migot, and N. Guelton: *Mater. Sci. Eng. A*, 2004, vols. 387–389, pp. 158-62.
9. Y.-K. Lee and C.-S. Choi: *Metall. Mater. Trans. A*, 2000, vol. 31A, pp. 355-60.
10. P.Y. Volosevich, V.N. Grindev, and Y.N. Petrov: *Phys. Met. Metallogr*., 1976, vol. 42, pp. 126-30.
11. R.E. Stoltz and J.B. Vander Sande: *Metall. Trans. A*, 1980, vol. 11A, pp. 1033-37.
12. V.G. Gavriljuk and H. Berns: *High Nitrogen Steels Structure, Properties, Manufacture, Applications*, Springer-Verlag, Berlin, 1999, pp. 58-62.
13. C.G. Rhodes and A.W. Thompson: *Metall. Trans. A*, 1977, vol. 8A, pp. 1901-06.
14. R.E. Schramm and R.P. Reed: *Metall. Trans. A*, 1975, vol. 6A, p. 1345.
15. P.C.J. Gallagher: *Metall. Trans*. 1970, vol. 1, pp. 2429-61.
16. B. Jiang, S. Yang, W. Zhou, and T.Y. Hsu: *Acta Mater*., 1998, vol. 46 (2), pp. 501-10.
17. V.G. Gavriljuk, H. Berns, C. Escher, N.I. Glavatskaya, A. Sozinov, and Y.N. Petrov: *Mater. Sci. Eng. A*, 1999, vol. 271, pp. 14-21.
18. Q.X. Dai, X.N. Cheng, X.M. Luo, and Y.T. Zhao: *Mater. Characterization*, 2003, vol. 49, pp. 367-71.
19. I.A. Yabuktsov, A. Ariapour, and D.D. Perovic: *Mater. Sci. Forum*, 1999, vol. 318–20, pp. 121-30.
20. I.A. Yabuktsov, A. Ariapour, and D.D. Perovic: *Acta Mater*., 1999, vol. 47 (47), pp. 1271-79.
21. Y. Petrov: *Naukova Dumka, Kiev*, 1978, p. 262 (in Russian).
22. M. De Meyer, D. Vanderschueren, K. De Blauwe, and B.C. De Cooman: *41st MWSP Conf. Proc*., ISS, Warrendale, PA, 1999, vol. 37, pp. 483-91.
23. J.B. Nelson and D.P. Riley: *Proc. Phys. Soc*., 1945, pp. 160-77.
24. G.B. Olson and M. Cohen: *Metall. Trans. A*, 1975, vol. 6A, pp. 791-95.
25. S.S. Hecker, M.G. Stout, K.P. Staudhammer, and J.L. Smith: *Metall. Trans. A*, 1982, vol. 13A, pp. 619-26.
26. J.-H. Jun and C.-S. Choi: *Mater. Sci. Eng. A*, 1998, vol. 257, pp. 353-56.
27. H. Schumann: *Neue Hütte*, 1972, vol. 17, pp. 605-09.
28. H.N. Han, C.G. Lee, C.-S. Oh, T.H. Lee, and S.-J. Kim: *Acta Mater*., 2004, vol. 52, pp. 5203-14.
29. J. Xuejun, Z. Jihua, and T.Y. Hsu: *Mater. Design*, 2000, vol. 21, pp. 537-39.
30. J.C. Li, M. Zhao, and Q. Jiang: *Metall. Mater. Trans. A*, 2000, vol. 31A, pp. 581-84.